Accepted Manuscript

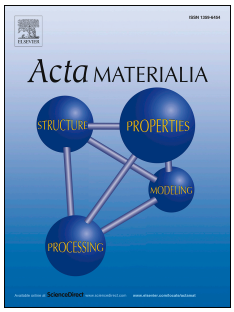

Metastable solidification pathways of undercooled eutectic CoSi–$CoSi_2$ alloys

Sangho Jeon, Matthias Kolbe, Victoria Kaban, Gabrielle String, Andre Cleaver, Ivan Kaban, Olga Shuleshova, Jianrong Gao, Douglas M. Matson

PII: S1359-6454(19)30422-7

DOI: https://doi.org/10.1016/j.actamat.2019.06.048

Reference: AM 15387

To appear in: *Acta Materialia*

Received Date: 14 March 2019

Revised Date: 21 June 2019

Accepted Date: 25 June 2019

Please cite this article as: S. Jeon, M. Kolbe, V. Kaban, G. String, A. Cleaver, I. Kaban, O. Shuleshova, J. Gao, D.M. Matson, Metastable solidification pathways of undercooled eutectic CoSi–$CoSi_2$ alloys, *Acta Materialia*, https://doi.org/10.1016/j.actamat.2019.06.048.

Graphical abstract

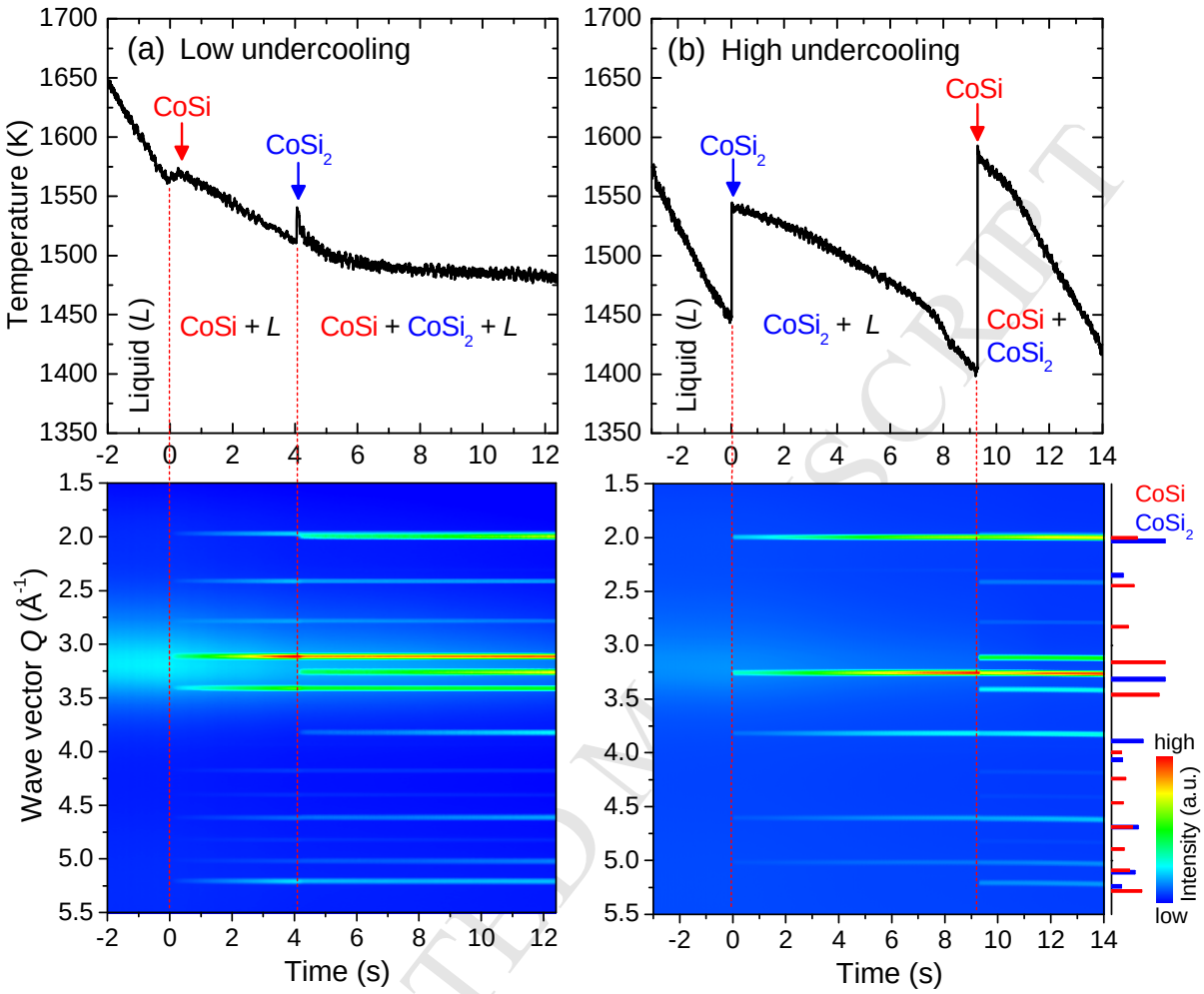

Metastable solidification pathways of undercooled eutectic CoSi–$CoSi_2$ alloys

Sangho Jeon[a], Matthias Kolbe[b], Victoria Kaban[c], Gabrielle String[a], Andre Cleaver[a], Ivan Kaban[c], Olga Shuleshova[c], Jianrong Gao[d], and Douglas M. Matson[a,*]

[a] Department of Mechanical Engineering, Tufts University, Medford, MA02155, USA

[b]Institut für Materialphysik im Weltraum, Deutsches Zentrum für Luft- und Raumfahrt (DLR), 51170 Koeln, Germany

[c]IFW Dresden, Institute for Complex Materials, Helmholtzstr. 20, 01069 Dresden, Germany

[d]Key Laboratory of Electromagnetic Processing of Materials (Ministry of Education), Northeastern University, Shenyang 110819, China

*Corresponding author. E-mail address: douglas.matson@tufts.edu

Abstract

Solidification and growth behavior of undercooled eutectic CoSi–$CoSi_2$ melts was observed using containerless levitation and *in situ* high-energy synchrotron X-ray diffraction techniques. Three metastable solidification pathways of eutectic CoSi–$CoSi_2$ were determined as a function of undercooling. Upon double recalescence at low undercoolings the primary and secondary phases are CoSi and $CoSi_2$, while at high undercoolings the phase formation sequence is reversed. At intermediate undercoolings a single recalescence was observed and attributed to a crossover of the nucleation barriers for the two phases. Scanning electron microscopy combined with electron back-scattering diffraction measurements revealed changes of the morphological characteristics and orientation of CoSi and $CoSi_2$ phases for different solidification pathways.

***Keywords*:** Eutectic Co–Si; Undercooling; Metastable solidification; *In situ* synchrotron X-ray diffraction; Electron back-scattering diffraction

1. Introduction

Rapid solidification of undercooled eutectic alloys has attracted considerable interest in past decades due to their unique competitive nucleation and growth mechanisms. In particular, many studies have been carried to understand non-equilibrium phenomena such as metastable solidification behavior and a morphological transition from regular lamellar eutectic to anomalous eutectic in a number of eutectic systems such as Ni–Sn [1–3], Ni–Si [4,5] Co–Sn [6,7], Ag–Cu [8,9], and Co–Si [10–14]. Solidification microstructures of those alloys have been shown to depend on experimental conditions. In addition to undercooling and cooling rates, levels of melt convection often differ using electrostatic levitation (ESL), electromagnetic levitation (EML), and glass-fluxing (GF) techniques [13–15]. The influence of these different experimental conditions was accomplished in past literature using thermal imaging of solidifying alloys and post-mortem microscopic analysis of solidified alloys [13]. Time-resolved X-ray diffraction (XRD) using synchrotron radiation has been performed to unambiguously determine metastable solidification pathways for undercooled Co–Si eutectic melts [12,14].

The Co–Si system includes five intermetallic compounds of α-Co_3Si, α-Co_2Si, β-Co_2Si, CoSi, and $CoSi_2$ [16,17]. Two compound-compound eutectics exist at Co–rich (Co_2Si–CoSi) and Si–rich (CoSi–$CoSi_2$) composition, respectively. Metastable solidification behavior for these systems has been investigated in the past using several different methods. Yao *et al*. reported an anomalous eutectic structure and divorced growth in Co_2Si–CoSi melt droplets using containerless drop-tube processing [11]. By means of microstructural studies and time-resolved XRD experiments, Wang *et al.* determined five solidification paths and identified two mechanisms for formation of anomalous eutectic in GF-processed melts of hypereutectic Co_2Si–CoSi composition [12]. For the CoSi–$CoSi_2$ eutectic, various containerless levitation techniques were applied to study phase selection and microstructure

formation in undercooled melts. A microstructural transition from lamellar eutectic to anomalous eutectic was observed in drop tube-processed samples of different sizes [10]. Using a combination of EML and synchrotron XRD, Li *et al*. demonstrated that upon solidification at deep undercoolings CoSi–$CoSi_2$ melts show double recalescence in which primary and secondary phases are $CoSi_2$ and CoSi, respectively [14]. Zhang *et al*. reported different growth kinetics of primary and secondary phases during double recalescence [13]. By comparing recalescence behavior observed under different melt convection conditions they suggested that melt convection has a significant effect on the incubation delay time between nucleation of a primary and a secondary phase based on experimental observations. However, it is not clear how the combined effects of convection and undercooling influence microstructural evolution in eutectic CoSi–$CoSi_2$ alloys, especially in light of the potential influence of constitutional undercooling and supersaturation [13,14]. Zhang *et al.* also proposed formation of an unknown metastable phase following primary growth of $CoSi_2$ in the mushy zone of Co–61.8 at. % Si melts [13]. However, approach and analysis for such phenomena are often difficult due to the influence of heterogeneous nucleation or the disruptive development of melt convection hindering attainment of deep undercooling or enhanced supersaturation of the melt, respectively.

In this work, solidification of undercooled eutectic CoSi–$CoSi_2$ (Co–61.8 at. % Si) alloys is studied using ESL techniques in order to attain quiescent melt conditions and systematically characterize structural evolution. In parallel, *in situ* synchrotron XRD experiments have been conducted on electromagnetically levitated samples to verify the sequence of phase formation as a function of undercoolings.

2. Experimental

$Co_{38.2}Si_{61.8}$ (at. %) alloys were prepared by arc-melting the pure elements (Co 99.95%, Si 99.995%, Alfa Aesar) under an Ar atmosphere. A zirconium sphere was used as an oxygen getter to scavenge the remained oxygen in the arc-melting chamber prior to melting of the constituents. The mass loss during the arc-melting process was less than 0.2% of the initial mass.

2.1 Electrostatic levitation

The ESL facility at the NASA Marshall Space Flight Center (MSFC) in Huntsville AL was used to study the rapid solidification behavior of quiescent melts. Samples with a mass of approximately 35 mg (a diameter of approx. 2 mm) were levitated between two electrodes and melted using a high voltage amplifier and a Nd-YAG high power laser under ultra-high vacuum (UHV) conditions of 10^{-7} Torr. The temperature of levitated samples was monitored with a Mikron MI-GA140 single-color pyrometer which is operated at a wavelength range of 1.45 – 1.8 μm. Each thermal cycle involved preheating, melting, and solidification of each sample. Before each cycle, the sample was thermally preconditioned to a temperature just below melting to ensure sample stability. Once levitated, the laser power was increased to induce melting and superheat the liquid. When the laser power was turned off the sample was allowed to freely cool by radiative heat loss until it fully solidified. Once several thermal cycles had been run on a given sample, testing was halted such that the evaporative loss was held to less than 2% of the initial mass.

2.2 *In situ* X-ray diffraction

Time-resolved *in situ* XRD measurements were conducted at the P07 high-energy material science beamline of the third-generation radiation source PETRA III at the Deutsches Elektronen-Synchrotron (DESY) in Hamburg [18] using an EML facility

developed by IFW Dresden. Samples with a mass of approximately 1.1 g (a diameter of approx. 6 mm) were placed in an UHV chamber backfilled to 450 mbar with high purity He gas after evacuation. Positioning and heating of EML samples were realized through use of a water-cooled copper coil powered by a 10 kW generator operating at 280 kHz. Active sample cooling was achieved by recirculation of the inert gas atmosphere (He) across the sample surface. The temperature of the levitated sample was monitored with a Mergenthaler single-color pyrometer operated at a wavelength range of 1.6 – 2.1 μm. Time-resolved, high-energy (E = 98 keV, λ = 0.1264 Å) XRD studies have been conducted in transmission mode using a hybrid pixel PILATUS3 X 2M CdTe detector (DECTRIS) at a sampling rate of 25 – 250 Hz. The recorded two-dimensional diffraction patterns were azimuthally integrated using the FIT2D software [19].

2.3 Microstructural analyses

Following completion of melt processing, the surface of the sample was observed using a Phenom ProX scanning electron microscope (SEM) (ThermoFisher Scientific) in back-scatter mode to identify regions for further study and determine how sectioning was to be accomplished. The preparation of the samples followed standard metallographic preparation rules: grinding with SiC sandpaper, polishing with a suspension of Al_2O_3 followed by polishing with an SiO_2 suspension of pH 9.8. The resulting cross section was near the center of each sample. The internal microstructure of the ESL processed samples was investigated using a Merlin SEM (Zeiss). Electron backscatter diffraction (EBSD) patterns were recorded in 70° tilt mode using an AZtecHKL EBSD-system with Nordlys Max^3 detector (Oxford Instruments). AZtecHKL software was used to index the recorded patterns and to visualize the results. The crystal structures used for indexing are taken from Pearson's crystal structure database for inorganic compounds entries 526854 (CaF_2-type

$CoSi_2$) and 452960 (FeSi-type CoSi). Three-dimensional morphology of the samples was studied by X-ray computed tomography (XCT) using a phoenix nanotom m CT system (GE Sensing & Inspection Technologies). Two-dimensional projection images of the samples were acquired using a tungsten X-ray source operating at the acceleration voltage of 130 kV and the current of 100 μA. The reconstruction and visualization of the volume models was done using phoenix datos|x2 (GE Sensing & Inspection Technologies), VGStudio (Volume Graphics), and VirtualDub [20] software.

3. Results and Discussion

3.1 Undercooling, delay time, and phase selection

Fig. 1 shows representative temperature-time profiles of Co–61.8 at. % Si alloys solidified with different degrees of undercooling in the ESL. The degree of undercooling ΔT was determined with a difference between the nucleation temperature of undercooled melts and the liquidus temperature T_L of the melt. In general, during levitation experiments a fraction of an undercooled melt solidifies under non-equilibrium conditions, causing rapid release of latent heat between solid and liquid phases accompanied by a characteristic recalescence event (sudden temperature rise). The remaining melt solidifies during post recalescence under conditions close to equilibrium. In Fig. 1a, at a low undercooling of 66 K the thermal profile shows not one, but two distinct temperature rise events (or double recalescence). A fraction of the melt first solidifies as a primary phase with subsequent solidification to a secondary phase after a delay time, τ, defined as the duration between the two recalescence events. The recalescence temperature of the secondary phase is slightly lower than that of the primary phase.

At intermediate undercoolings, the thermal profiles typically exhibit three types of behavior as shown in Fig. 1b. The first behavior mode is double recalescence where the slope

of the cooling curve following primary recalescence is distinctly different from that detected at low undercoolings, implying a change of the primary solidifying phase as indicated by the black line in Fig. 1b. In addition, the recalescence temperature of the secondary phase exceeds the bulk sample liquidus. This thermal anomaly is associated with a sudden drop in temperature during the melting stage of the subsequent heating curve and can be attributed to a shift of the phase-specific emissivity [21]. The second behavior mode involves double recalescence combined with a short delay time. During this rare case, shown as the blue line in Fig. 1b, the strong recalescence of the secondary phase is not observed. The third behavior mode involves a single recalescence at intermediate undercoolings as indicated with the red line in Fig. 1b. These three solidification behaviors occur randomly in the intermediate undercooling range between 100 K and 150 K. At undercoolings higher than about 150 K (Fig. 1c), the thermal profiles show a double recalescence which is similar to that observed at intermediate undercoolings. However, prior to nucleation of the secondary phase the temperature profile exhibits a small hump (see arrow in Fig. 1c). This hump begins at a narrow band of temperatures just prior to initiation of the second recalescence.

Fig. 2 shows a relation between the undercooling ΔT and delay time τ obtained from the temperature-time profiles. At low undercoolings, the delay time decreases with increasing undercooling. This is consistent with nucleation and growth models involving a competition between stable and metastable phases; such behavior is also reported for other alloy systems which exhibit double recalescence [22,23]. However, the delay time shows a large scatter in the range of 0 to 12 s at intermediate undercoolings. The delay time decreases again at high undercoolings, but its initial value is much higher than observed at low undercoolings.

Zhang *et al*. reported that the delay time of Co–61.8 at. % Si alloys depends on experimental conditions [13]; at undercooling regions of ~ 150 K, the delay times do not exceed 2 s for samples processed by EML but are 3.765 s and 0.94 s at undercoolings of 122

K and 222 K for samples processed by EML with static magnetic field, respectively. In other work [14], the delay time of Co–61.8 at. % Si alloys using EML was about 9.6 s at an undercooling of 140 K. These previous results imply that the transformation delay time depends on the level of melt convention induced by different experimental techniques [24,25]. The intensity of melt flow would also depend on the volume fraction of primary solid. In the current work, all the alloys are free from the flow induced by an electromagnetic force and are characterized by quiescent conditions. Marangoni melt convection driven by a temperature gradient of about 5 K would initially be weak during melting; during solidification the flow would dampen to zero. Therefore, it could be assumed that the relation between undercooling and delay time in Fig. 2 is the result of a combination between growth of the primary phase and nucleation of the secondary phase under near homogeneous nucleation condition. On the basis of these points, the three distinct regions of delay time behavior imply that eutectic CoSi−$CoSi_2$ may follow three metastable solidification pathways depending on the sample undercooling in the absence of melt convection. In the following text, the three pathways are referred to as pathway I, II, and III, and the undercooling range where each pathway is observed is marked by gray, yellow, and green highlights, respectively.

Previous studies showed that at high undercoolings the primary and secondary phases are $CoSi_2$ and CoSi, respectively based on *in situ* synchrotron XRD experiments [14] and microstructure evaluation [13,14]. It was also demonstrated that the phase formation sequence is reversed at low undercoolings based on microstructure evaluations [13,14]. In order to have more insights into the reversal of the phase formation sequence, *in situ* time-resolved synchrotron XRD experiments for a Co–61.5 at. % Si alloy were conducted using EML at the German synchrotron facility DESY, and the *in situ* XRD evolution plots at low and high undercoolings are shown in Fig. 3a and b, respectively. The corresponding thermal

profile during cooling (top panel) is synchronized in time with the XRD spectra (bottom panel) which are presented as an intensity map. In the undercooled liquid region, both XRD profiles exhibit a characteristic broad spectrum typical of liquid structures. Upon solidification distinct Bragg peaks emerge against the diffuse intensity of the liquid. At a low undercooling (Fig. 3a), the peaks are identified as the spectrum of CoSi with an FeSi-type *B*20 structure. A gradual increase in the diffraction intensity indicates an increase of the volume fraction of the primary CoSi phase in the remaining melt. After a delay time of about 4 s, new Bragg peaks appear aligned with a corresponding temperature rise on the temperature-time profile; the peaks are identified as the spectrum of $CoSi_2$ with a CaF_2-type *C*1 structure. At a high undercooling (Fig. 3b), the phase formation sequence is reversed. These XRD results clearly demonstrate the phase formation sequences for eutectic CoSi–$CoSi_2$ melts at low and high undercoolings and are consistent with the observations of changes in the slope of the cooling curve from pyrometry data.

Phase competition for primary nucleation in undercooled melts can be attributed to a nucleation controlled or a growth controlled mechansim [26]. According to the work by Zhang *et al*. [13], the growth velocities of CoSi are by one order of magnitude of higher than those of $CoSi_2$ in metastable solidification of eutectic CoSi–$CoSi_2$ alloys, no matter which phase is a primary phase. For that huge difference, those researchers suggested that the phase competition in undercooled CoSi–$CoSi_2$ melts is controlled by a competitive nucleation mechanism, rather than by a competitive growth mechanism. It means that the crystal-melt interfacial free energy for CoSi and CoSi nuclei in the undercooled melt would play a decisive role in determining the primary nucleation phase. However, quantitative analysis for the primary phase selection with undercooling is challenging since the crystal-melt interfacial free energy of both phases is temperature-dependent and is a function of how the local structural similarity between the liquid and two phases changes with undercooling [27–29].

Here, we approach qualitatively the origin of the metastable solidification behavior within the three solidification pathways.

Fig. 4a illustrates a partial phase diagram of the Co–Si system [16]. Solid lines represent the equilibrium liquidus; red and blue dashed lines indicate the projected extension of the liquidus for CoSi and $CoSi_2$ in the undercooled region, respectively. In both parts of Fig. 4 the three solidification pathway regions are highlighted by color (primary CoSi – gray, mixed – yellow, primary $CoSi_2$ – green). In the eutectic CoSi–$CoSi_2$, the growth of a primary phase causes a difference between solute concentrations of the remaining melt and the initially undercooled bulk melt and thus involves a constitutional undercooling of the remaining melt which is proportional to the thermodynamic driving force for nucleation of a second phase. Meanwhile, the solute concentration difference between the remaining melt and the second phase could affect the crystal-melt interfacial free energy [29,30]. In order to quantify both contributions to the nucleation of the second phase, we first calculated a fraction of primary solid (f_s) as a function of undercooling by the Stefan Equation:

$$C_p \Delta T = f_s \Delta H_f \quad (1)$$

where C_p is the specific heat of the bulk melt at constant pressure, ΔT is the bulk undercooling, and ΔH_f is the heat of fusion of the primary solid. With knowledge of the fraction solid, the composition of the remaining melt can be deduced as a function of undercooling using the lever rule for primary growth of either CoSi or $CoSi_2$. In order to simplify this approach, we assume that the interfacial undercooling derived by the compositionally imposed change contributes largely to the thermodynamic driving force, and the solute concentration difference between the remaining melt and the second phase is proportional to the crystal-melt interfacial free energy. Hence the thermodynamic driving

force (ΔT_i) and the solute concentration difference (ΔC_i) with primary solid are simply defined as follows

$$\Delta T_i = (T_L - T_s), \quad \Delta C_i = |C_L - C_s| \quad (i = CoSi, CoSi_2) \tag{2}$$

where T_L and T_s are the liquidus and solid temperatures at the solid-liquid interface, respectively, and C_L and C_s are the Si concentrations of the remaining melt and second phase, respectively. The subscript i refers to either CoSi or $CoSi_2$ as the primary phase. Using the literature values for C_p of 31.34 J K^{-1} mol^{-1} (bulk melt) [10] and ΔH_f of 19473 J mol^{-1} (CoSi) and 26653 J mol^{-1} ($CoSi_2$) [31], the ΔT_i and the absolute value of ΔC_i were calculated as a function of initial undercooling and are illustrated in Fig. 4a for cases of primary nucleation of CoSi (ΔT = 100 K) and $CoSi_2$ (ΔT = 150 K). These cases are shown on the diagram by curved arrows connecting the primary undercooling to the predicted equilibrium temperature based on the apparent composition shift in liquid composition. The shift in composition for primary CoSi is significant while the shift for $CoSi_2$ is not.

The limits of physical behavior can now be evaluated by defining the fraction solid that must form to shift the composition from the eutectic to a liquid of composition equivalent to either of the pure compounds; from that the undercooling required to cause this composition shift to occur may be defined. Following the primary growth of CoSi, the remaining melt becomes Si-rich liquid and the atomic composition of the melt reaches 66.67% Si (equivalent to $CoSi_2$) at a fraction solid of 0.291 with a projected hypothetical undercooling of 181 K. On the other hand, the atomic composition of the remaining melt becomes Co-rich liquid during the primary growth of $CoSi_2$ and reaches equimolar composition (equivalent to CoSi) at a fraction solid of 0.709 with a projected hypothetical undercooling of 603 K which was not accessed during real rapid solidification processing.

In Fig. 4b, the primary nucleation of CoSi rapidly increases the ΔT_{CoSi} with increasing undercooling; this promotes conversion to the second phase. The delay time for nucleation of the second phase should be short and get shorter with increasing undercooling. Meanwhile, the primary nucleation of $CoSi_2$ causes a consistently larger ΔC_{CoSi2} thus slowing nucleation of the second phase due to the high crystal-melt interfacial free energy, resulting in long delay times. Both of these effects are evident in Fig. 2.

From the classical nucleation theory (CNT) one may expect that there is a crossover point where the nucleation barriers of the two phases are equal at some intermediate undercooling [13]. This would allow the CoSi and $CoSi_2$ phases to nucleate and grow simultaneously such that only a single recalescence would be observed at intermediate undercoolings. At temperatures that deviate to either side of the crossover point, CoSi or $CoSi_2$ could nucleate first as a primary phase. The primary nucleation of CoSi should involve an immediate nucleation of $CoSi_2$ due to the higher driving force as shown in Fig. 4b and thus the primary growth of CoSi is hard to observe at intermediate undercoolings (Fig. 1b). During the primary nucleation and growth of $CoSi_2$, the second phase could be occasionally facilitated by heterogeneous nucleation sites, and therefore the observed scatter of delay times at intermediate undercooling in Fig. 2 may be a result of the statistical nature of nucleation events.

Analysis of the characteristic nucleation and recalescence temperature data suggests an alternative explanation of the origin of the delay time dependency on undercooling for the case of the primary nucleation of the $CoSi_2$ phase (Fig. 5). Apparently, when the volume fraction of the $CoSi_2$ phase exceeds some critical value, nucleation of the CoSi phase is hindered. This happens despite the fact that residual liquid composition shifts towards the equi-atomic composition, as shown in Fig. 4, and could be caused by an effective reduction of the potency of heterogeneous nucleation cites present in the liquid (e.g. preferential

dissolution of oxides). Therefore, after recalescence the $CoSi_2$ + liquid mixture continues to cool down until the system reaches some critical nucleation temperature with a corresponding fraction of solid and liquid phases each at a characteristic composition. As undercooling increases, the volume fraction of the $CoSi_2$ phase formed during the recalescence event increases. From this point onward, the cooling process is relatively independent of the initial undercooling (except for any residual internal morphology characterized by the size of the $CoSi_2$ primary dendrites) and the solidification rate is thus determined by the heat extraction rate and the equilibrium slope from the phase diagram. The delay time, however, would be shorter as it would take less time for the sample to attain the same critical temperature.

3.2 Microstructure analysis

Five ESL samples were selected for analysis to investigate changes in the morphological characteristics and orientation of CoSi and $CoSi_2$ phases for the three solidification pathways. Fig. 6 shows the morphology of a representative sample exhibiting Pathway-I delay behavior. Fig. 6a and b show the EBSD orientation maps colored for CoSi and $CoSi_2$ phases for a sample marked as PW I in Fig. 2, respectively. The microstructure of the CoSi phase consists of three types: fine and rod-like (or rounded) particles in the edge region and fully developed dendrites in the central region of the sample. Some of the CoSi particles are enveloped by equiaxed $CoSi_2$ grains. Such microstructure patterns also demonstrate that the primary phase is CoSi for pathway I. The fully developed CoSi dendrites are embedded in the matrix of $CoSi_2$ grains. They appear to have grown toward the sample center under the influence of a radial temperature gradient after multiple nucleation at the sample surface. A small amount of eutectic is discerned only near grain boundary areas of $CoSi_2$. The (100) pole figure of the CoSi phase shows a fully random texture without any preferential orientation (Fig. 6c), meaning that dendrites grew from different nucleation sites

across the sample surface. In contrast, the (100) pole figure of the $CoSi_2$ phase shows a highly ordered texture with preferred diffraction orientation (Fig. 6d).

Fig. 7 shows the morphology of samples exhibiting Pathway-II delay behavior. Fig. 7a and b show the EBSD orientation maps colored for CoSi and $CoSi_2$ phases of a sample marked as PW II-a in Fig. 2, respectively. Note that crystallographic regions of similar orientation are shown in the same color. Fine and rounded CoSi particles are observed in the edge and central regions of the sample, respectively. The $CoSi_2$ phase exhibits equiaxed grains with mixed orientation, and the grain size in the edge region is smaller than that in the center. Unlike the case of pathway I, the CoSi particles are embedded in the matrix of equiaxed $CoSi_2$ grains and fully developed dendrites of CoSi are not found. In addition, a small amount of eutectic is observed in the $CoSi_2$ grains, indicating concurrent post-recalescence growth of both CoSi and $CoSi_2$. The (100) pole figures of the both phases show no discernable texture (Fig. 7c and d).

Morphological characteristics of the microstructure of samples change remarkably between samples involving short and long delay time within pathway-II. Fig. 7e and f show the EBSD orientation maps colored for $CoSi_2$ and CoSi phases of a sample marked as PW II-b in Fig. 2, respectively, representing the long delay behavior. The microstructure of the sample is dominated by equiaxed $CoSi_2$ grains, and large plate-like layer of $CoSi_2$ with a common orientation is observed along the exterior surfaces of the sample. Because the edge region is expected to solidify first, the primary phase must be $CoSi_2$ for this pathway. An interconnected network of CoSi with a small fraction of regular eutectics is distributed along the boundary of the $CoSi_2$ grains. Regular eutectic structures are observed in a region close to the sample surface. They are formed by isothermal solidification after re-melting of the primary $CoSi_2$ phase due to the recalescence of CoSi [32]. The (100) pole figure of the $CoSi_2$

phase does not show any strong texture (Fig. 7g), but the secondary CoSi grains are partially aligned (Fig. 7h) in a fibrous texture.

Fig. 7i and j show the EBSD orientation maps colored for $CoSi_2$ and CoSi phases of a sample marked as PW II-c in Fig. 2, respectively. The microstructure of the sample is also dominated by equiaxed $CoSi_2$ grains, but the large single plate-like $CoSi_2$ layer along the exposed surface is not found. The intergranular regions also constitute an interconnected network of CoSi and show good wetting to the $CoSi_2$ grains. A small amount of regular eutectics is found near the intergranular regions. The $CoSi_2$ grains are partially aligned as shown in Fig. 7k whereas the CoSi grains are almost randomly oriented (Fig. 7l).

Fig. 8 shows the morphology of a representative sample exhibiting Pathway-III delay behavior. Fig. 8a and b show the EBSD orientation maps colored for $CoSi_2$ and CoSi phases of a sample marked as PW III in Fig. 2, respectively. The $CoSi_2$ grains look dendritic more than equiaxed, but the microstructural aspects of the CoSi phase do not show remarkable change as compared to structures observed in Fig. 7j. Interestingly, the (100) pole figure of the $CoSi_2$ phase shows a highly oriented texture (Fig. 8c), which is consistent with the previous results [13]. The secondary CoSi grains are partially oriented but to a lesser degree than the primary $CoSi_2$ (Fig. 8d).

Tomography scans for 3D morphologies of the samples of pathways I (Fig. 6) and II-c (Fig. 7) were conducted to support the microstructural observations (see supplementary videos 1 and 2) and reveal the three-dimensional morphology of the sample interior. Fig. 9a and b show a captured image from the tomography scan and a back-scatter SEM image for the surface of the sample of pathway I, respectively, and those for pathway II-c are shown in Fig. 9c and d, respectively. The sample surface for pathway I exhibits a region with planar plate-like features with CoSi particles and $CoSi_2$ grains showing light and dark contrast, respectively. However, a dramatic change is observed on the sample surface for pathway II-c

which shows a cellular-like structure. This structure is formed by constitutional undercooling of the melt caused by solute rejection during the primary growth of $CoSi_2$ and observed on all the samples with long delay time [21,33]. This means that the formation of cellular structure is closely related to the degree of constitutional undercooling. Small dots along the top surfaces of the cellular features in Fig. 9d are confirmed to be residual regions of CoSi which were isolated from the bulk melt prior to secondary recalescence.

3.3 Effect of supersaturation of $CoSi_2$

As discussed in Section 3.1, a small hump is observed before the secondary nucleation of CoSi at high undercoolings and seems to appear when the undercooling exceeds a critical point. Two interpretations are possible: one is an emissivity change due to morphology of the surface structure, and the other is an emissivity change due to crystal structure relaxation of supersaturation within the primary phase. In general, the emissivity of solid and liquid phases is dependent on their extrinsic and intrinsic properties, respectively. As shown in Fig. 9c, the cellular structure exhibits a non-planar view factor that may cause an emissivity increase. The degree of emissivity change depends on the surface roughness which results from decanting of surface liquid as the sample solidifies. This decanting is related to the local undercooling [21]. However, the temperature range at which the small hump appears (see arrow in Fig. 1c) and the delay time corresponding to the small hump depend little on the local undercooling. In an extreme example, the cellular structure is seen even in samples at high undercoolings but where no hump is observed. Therefore, the correlation between the small hump and the emissivity change by surface roughness is considered unlikely.

In contrast, observations of the small hump seem to correlate with the approach to a specific atomic composition of the remaining melt, which is equivalent to reaching a specific

saturation temperature composition as shown in Fig. 1c. The hump may thus be related to recrystallization or solute rejection from the now-superheated parent phase. To investigate this hypothesis, we measured thermal cycles of pure CoSi and pure $CoSi_2$ compounds using the same ESL techniques as employed for the eutectic mixture. Fig. 10 shows a comparison of the temperature-time profiles of (a) pure CoSi, (b) eutectic CoSi–$CoSi_2$ (Co–61.8 at. % Si), and (c) pure $CoSi_2$ samples where the liquidus temperature of each material is marked by a red dotted line. The recalescence temperature of the CoSi alloy exceeds the liquids (Fig. 10a). This is due to an emissivity change between solid and liquid phases which is probably caused by the small fraction of covalent bonds between Co and Si atoms in the CoSi *B*20 structure [34,35]. This implies that the strong secondary recalescence of CoSi in Fig. 10b may be related to an emissivity change involving CoSi. Post recalescence, the CoSi alloy cools down without any solid-solid phase transformation, as expected from the Co–Si phase diagram [16,17].

For solidification of the pure $CoSi_2$ alloy a small peak is unexpectedly observed near 1460 K as marked by an arrow in Fig. 10c. The peak corresponds to a kink or a slope change around 1460 K in the thermal profile on the subsequent heating cycle as shown in the inset in Fig. 10c. This behavior is not expected to occur based on analysis of the equilibrium phase diagram. The occurrence of the small peak depends on facility-specific experimental conditions as it is seen in ESL but not in EML. Fig. 11 shows a continuous series of thermal cycles of a single sample of $CoSi_2$ in the ESL – by doing the processing over an extended time it is possible to intentionally shift the composition due to preferential evaporation of the more volatile species (it is Co here). In the first five cycles the small peak is not observed. However, at the 6th cycle a small peak appears (see arrow in Fig. 11) and it becomes more pronounced as the thermal cycles are subsequently repeated. After completion of all thermal cycles, the sample showed a total mass loss of 3.9%. It is well known that the vapor pressure

of elemental Co is greater than that of Si at high temperatures [36]. Hence, the bulk composition of the $CoSi_2$ alloy was shifted over the course of the experiments to a more Si-rich composition, leading to formation of a tiny fraction of hypoeutectic $CoSi_2$–Si and during cooling, this leads to the peak. Note that in Fig. 10b and c the temperatures at which the small hump and the small peak occur are very similar. Therefore, the small hump in eutectic CoSi–$CoSi_2$ alloy may be related to a slight compositional change of supersaturated $CoSi_2$ during metastable solidification in the mushy zone. The detailed correlation between the compositional change and the degree of supersaturation should be developed in the future to confirm this hypothesis.

4. Conclusions

In summary, the solidification pathways of Co–61.8 at. % Si melts have been investigated using ESL in combination with *in situ* time-resolved XRD diagnosis. Three different pathways have been identified to describe how the delay time between primary and secondary phase formation depends on bulk undercooling for eutectic CoSi–$CoSi_2$. *In situ* synchrotron XRD experiments have confirmed that during double recalescence the primary and secondary phases are CoSi and $CoSi_2$ at low undercoolings, and the phase formation sequence is reversed at high undercoolings. Microstructural evaluations support the observations from pyrometry and time-resolved XRD for the sequence of phases formed. A single recalescence is seen at intermediate undercoolings and this behavior is attributed to the existence of a cross-over point where the nucleation barriers of CoSi and $CoSi_2$ are similar in the undercooled region. At high undercoolings, a small hump appears before the secondary nucleation of CoSi in the mushy zone when the undercooling of melts exceeds a critical point. This behavior is consistent with a structurally-dependent emissivity shift. The results

have shown that the undercooling, transformation delay time, and stirring each can play an important role in determining metastable solidification pathways for eutectic melts.

Acknowledgements

We would like to thank Trudy L. Allen and Glenn Fountain for technical assistance at NASA Marshall Space Flight Center (MSFC) and O. Gutowski, A.-C. Dippel, and M. v. Zimmermann for experiment support at DESY in using the high-energy materials science beamline P07. For technical support with the X-ray computed tomography at IFW Dresden authors would like to thank A. Funk. The work at Tufts University was partially funded by NASA, under the ELFSTONE grants NNX16AB59G and 80NSSC19K0256. The work at DLR was partially funded by ESA MAP LIPHASE No. 4200015005/01/NL/SH. The work at IFW Dresden was funded by DLR project PARMAG (contract number 50WM1546) and by ESA MAP Project MAGNEPHAS AO-99-101 (contract number 4200014980).

References

[1] B. Wei, G. Yang, Y. Zhou, High undercooling and rapid solidification of Ni–32.5% Sn eutectic alloy, Acta Metall. Mater. 39 (1991) 1249–1258.

[2] C. Yang, J. Gao, Y.K. Zhang, M. Kolbe, D.M. Herlach, New evidence for the dual origin of anomalous eutectic structures in undercooled Ni–Sn alloys: In situ observations and EBSD characterization, Acta Mater. 59 (2011) 3915–3926.

[3] J.F. Li, W.Q. Jie, S. Zhao, Y.H. Zhou, Structural evidence for the transition from coupled to decoupled growth in the solidification of undercooled Ni–Sn eutectic melt, Metall. Mater. Trans. A 38 (2007) 1806–1816.

[4] F. Zhang, C. Lai, J. Zhang, Y. Zhang, Q. Zhou, H. Wang, Anomalous eutectics in intermediately and highly undercooled Ni–29.8 at. % Si eutectic alloy, J. Cryst. Growth 495 (2018) 37–45.

[5] C. Lai, H. Wang, Q. Pu, T. Xu, J. Yang, X. Zhang, F. Liu, Phase selection and re-melting-induced anomalous eutectic in undercooled Ni–38 at. % Si alloy, J. Mater. Sci. 51 (2016) 10990–11001.

[6] L. Liu, J.F. Li, Y.H. Zhou, Solidification interface morphology pattern in the undercooled Co–24.0 at. % Sn eutectic melt, Acta Mater. 59 (2011) 5558–5567.

[7] L. Liu, X.X. Wei, Q.S. Huang, J.F. Li, X.H. Cheng, Y.H. Zhou, Anomalous eutectic formation in the solidification of undercooled Co–Sn alloys, J. Cryst. Growth 358 (2012) 20–28.

[8] C.R. Clopet, R.F. Cochrane, A.M. Mullis, The origin of anomalous eutectic structures in undercooled Ag–Cu alloy, Acta Mater. 61 (2013) 6894–6902.

[9] S. Zhao, J. Li, L. Liu, Y. Zhou, Eutectic growth from cellular to dendritic from in the undercooled Ag–Cu eutectic alloy melt, J. Cryst. Growth 311 (2009) 1387–1391.

[10] W.J. Yao, N. Wang, B. Wei, Containerless rapid solidification of highly undercooled Co–Si eutectic alloys, Mater. Sci. Eng. A 334 (2003) 10–19.

[11] W. Yao, Z. Ye, N. Wang, X. Han, J. Wang, X. Wen, Competitive nucleation and rapid growth of Co–Si intermetallic compounds during eutectic solidification under containerless processing condition, J. Mater. Sci. Technol. 27 (2011) 1077–1082.

[12] Y. Wang, J. Gao, M. Kolbe, A. Chuang, Y. Ren, D.M. Matson, Metastable solidification of hypereutectic Co_2Si–CoSi composition: Microstructural studies and in-situ observations, Acta Mater. 142 (2018) 172–180.

[13] Y.K. Zhang, J. Gao, M. Kolbe, S. Klein, C. Yang, H. Yasuda, D.M. Herlach, Ch.-A. Gandin, Phase selection and microstructure formation in undercooled Co–61.8 at. % Si melts under various containerless processing conditions, Acta Mater. 61 (2013) 4861−4873.

[14] M. Li, K. Nagashio, T. Ishikawa, A. Mizuno, M. Adachi, M. Watanabe, S. Yoda, K. Kuribayashi, Y. Katayama, Microstructure formation and in situ phase identification from undercooled Co–61.8 at. % Si melts solidified on an electromagnetic levitator and an electrostatic levitator, Acta Mater. 56 (2008) 2514–2525.

[15] M. Li, T. Ishikawa, K. Nagashio, K. Kuribayashi, S. Yoda, A comparative EBSP study of microstructure and microtexture formation from undercooled $Ni_{99}B_1$ melts solidified on an electrostatic levitator and an electromagnetic levitator, Acta Mater. 54 (2006) 3791–3799.

[16] K. Ishida, T. Nishizawa, M.E. Schlesinger, The Co–Si (Cobalt–Silicon) system, J. Phase Equilibria 12 (1991) 578–586.

[17] L. Zhang, Y. Du, H. Xu, Z. Pan, Experimental investigation and thermodynamic description of the Co–Si system, CALPHAD 30 (2006) 470–481.

[18] N. Schell, A. King, F. Beckmann, T. Fischer, M. Mueller, A. Schreyer, The high energy materials science beamline (HEMS) at PETRA III, Mater. Sci. Forum 772 (2014) 57–61.

[19] A.P. Hammersley, S.O. Svensson, M. Hanfland, A.N. Fitch, D. Häusermann, Two-dimensional detector software: from real detector to idealised image or two theta scan, High Pressure Res. 14 (1996) 235–248.

[20] <https:// www.virtualdub.org/>.

[21] S. Jeon, D.M. Matson, Formation of cellular structure on metastable solidification of undercooled eutectic CoSi–62 at. %, Crystals 7 (2017) 295.

[22] R.W. Hyers, D.M. Matson, K.F. Kelton, J.R. Rogers, Convection in containerless processing, Ann. NY Acad. Sci. 1027 (2004) 474–494.

[23] K. Eckler, F. Gärtner, H. Assadi, A.F. Norman, A.L. Greer, D.M. Herlach, Phase selection, growth, and interface kinetics in undercooled Fe–Ni melt droplets, Mater. Sci. Eng. A 226–228 (1997) 410–414.

[24] D.M. Matson, R.W. Hyers, T. Volkmann, H.-J. Fecht, Phase selection in the mushy-zone: *LODESTARS* and *ELFSTONE* Projects, J. of Phys. 327 (2011) 012009.

[25] D.M. Matson, X. Xiao, J.E. Rodriguez, J. Lee, R.W. Hyers, O. Shuleshova, I. Kaban, S. Schneider, C. Karrasch, S. Burggraff, R. Wunderlich, H.-J. Fecht, Use of thermophysical properties to select and control convection during rapid solidification of steel alloys using electromagnetic levitation on the space station, JOM 69 (2017) 1311–1318.

[26] M. Li, S. Ozawa, K. Kuribayashi, On determining the phase-selection principle in solidification from undercooled melts–competitive nucleation or competitive growth, Phil. Mag. Lett. 84 (2004) 483–493.

[27] F. Spaepen, A structural model for the solid-liquid interface in monoatomic system, Acta Metall. 23 (1975) 729–743.

[28] Z. Jian, N. Li, M. Zhu, J. Chen, F. Chang, W. Jie, Temperature dependence of the crystal-melt interfacial energy of metals, Acta Mater. 60 (2012) 3590–3603.

[29] F. Spaepen, Homogeneous nucleation and the temperature dependence of the crystal-melt interfacial tension, Solid State Phys. 47 (1994) 1–32.

[30] I. Shimizu and Y. Takei, Temperature and compositional dependence of solid-liquid interfacial energy: application of the Cahn–Hilliard theory, Physica B 362 (2005) 169–179.

[31] W.J. Yao, N. Wang, Latent heats of fusion and crystallization behaviors of Co–Si binary alloys, J. Alloy. Compd. 487 (2009) 354–357.

[32] X.X. Wei, X. Lin, W. Xu, Q.S. Huang, M. Ferry, J.F. Li, Y.H. Zhou, Remelting-induced anomalous eutectic formation during solidification of deeply undercooled eutectic alloy melts, Acta Mater. 95 (2015) 44–56.

[33] K.G. Prashanth, J. Eckert, Formation of metastable cellular microstructure in selective laser melted alloys, J. Alloy. Compd. 707 (2017) 27–34.

[34] L. Pauling, A.M. Soldate, The nature of the bonds in the iron silicide FeSi, and related crystals, Acta Cryst. (1948) 212–216.

[35] A.I. Al-Sharif, M. Abu-Jafar, A. Qteish, Structural and electronic structure properties of FeSi: the driving force behind the stability of the B20 phase, J. Phys.: Condens. Matter 13 (2001) 2807–2815.

[36] R.E. Honig, D.A. Kramer, Vapor pressure data for the solid and liquid elements, RCA Rev. 30 (1969) 285–305.

579 **Figure 1**

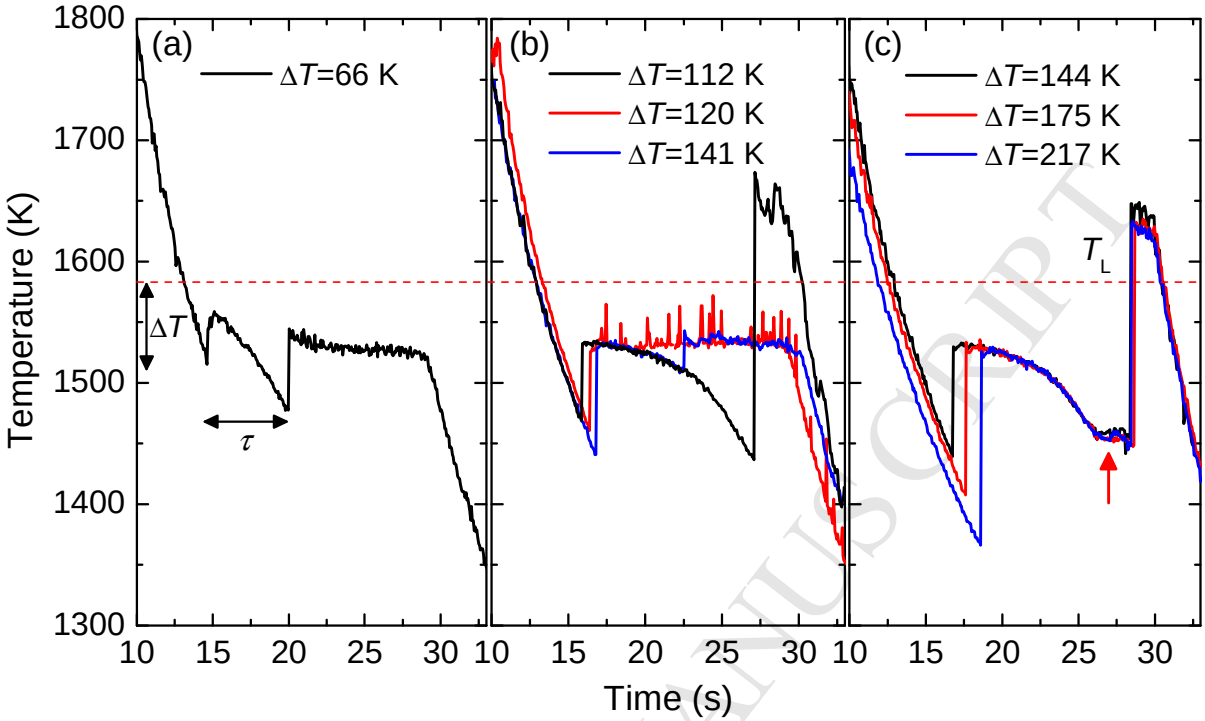

580
581 Fig. 1. Temperature-time profiles of Co–61.8 at. % Si alloys at (a) low, (b) intermediate, and
582 (c) high undercoolings in the ESL experiments. The liquidus temperature T_L (dashed line)
583 was determined based on the Co–Si phase diagram [16].

584 **Figure 2**

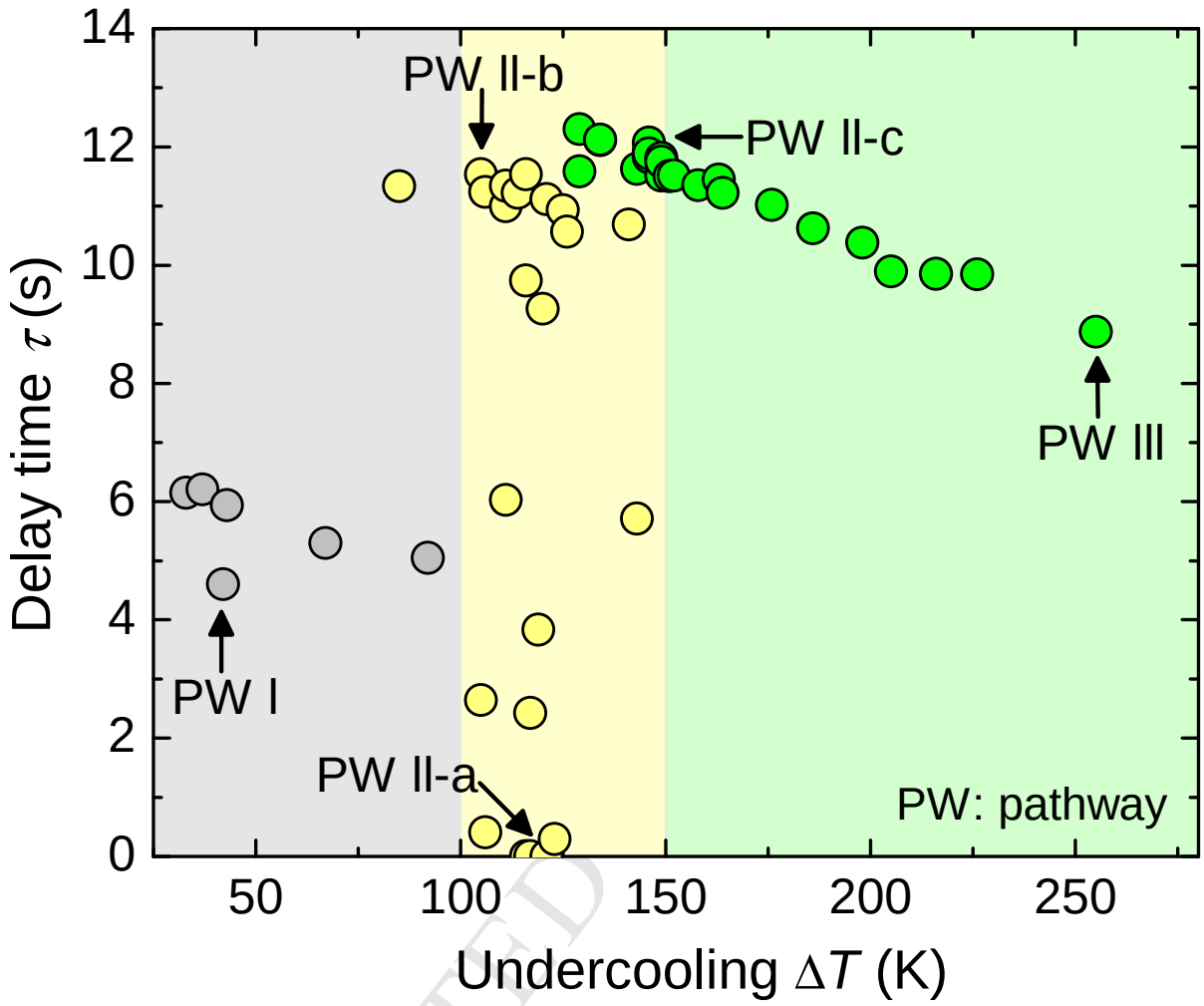

585

586 Fig. 2. Relation between undercooling ΔT and delay time τ of Co–61.8 at. % Si alloys in the

587 ESL.

588

589 **Figure 3**

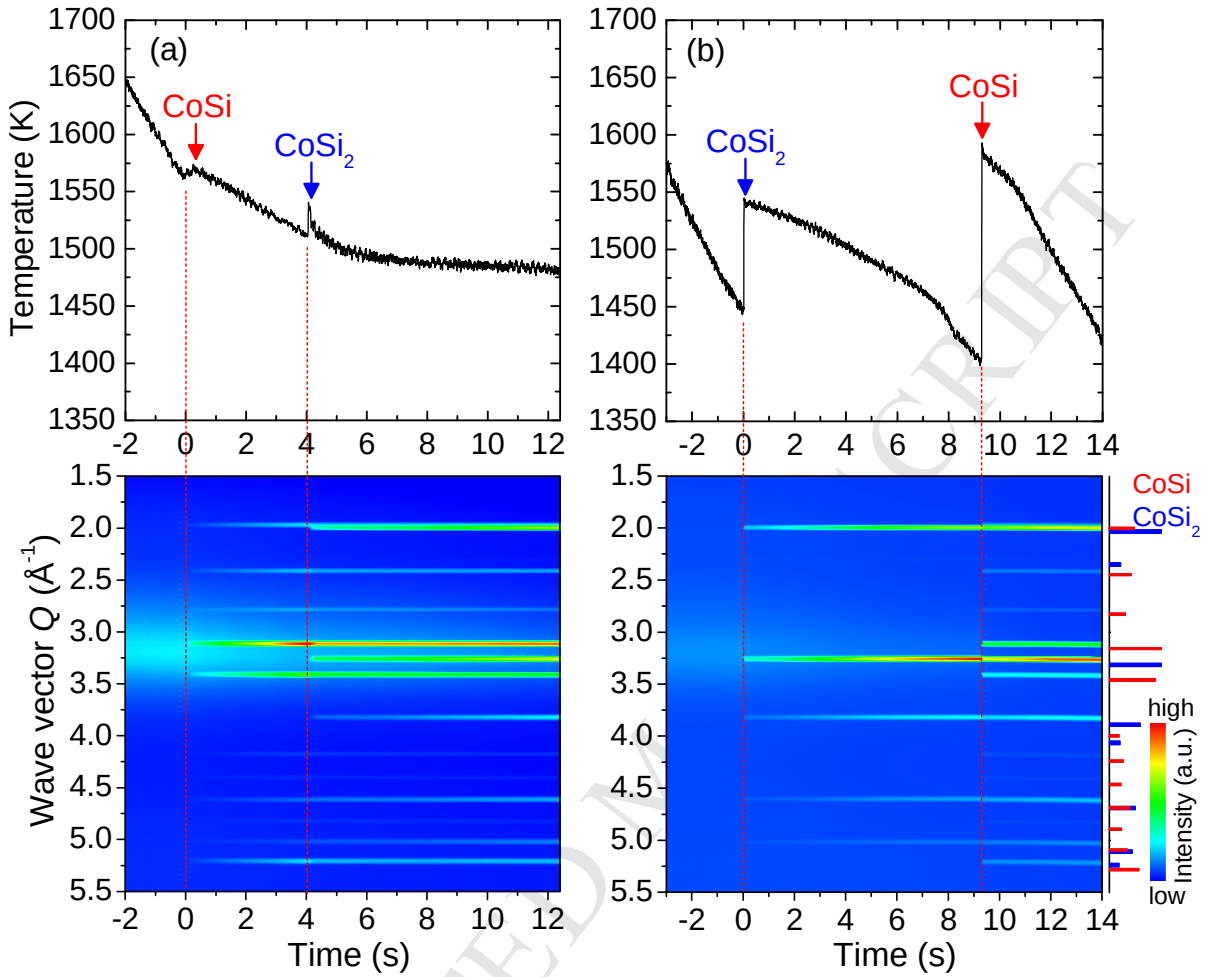

590

591 Fig. 3. Time evolution of temperature (Top) and XRD spectra (bottom) of a Co–61.5 at. % Si

592 melt at (a) low and (b) high undercoolings in the EML. The Bragg peaks of crystalline phases

593 were assigned in the right panel.

594

595 **Figure 4**

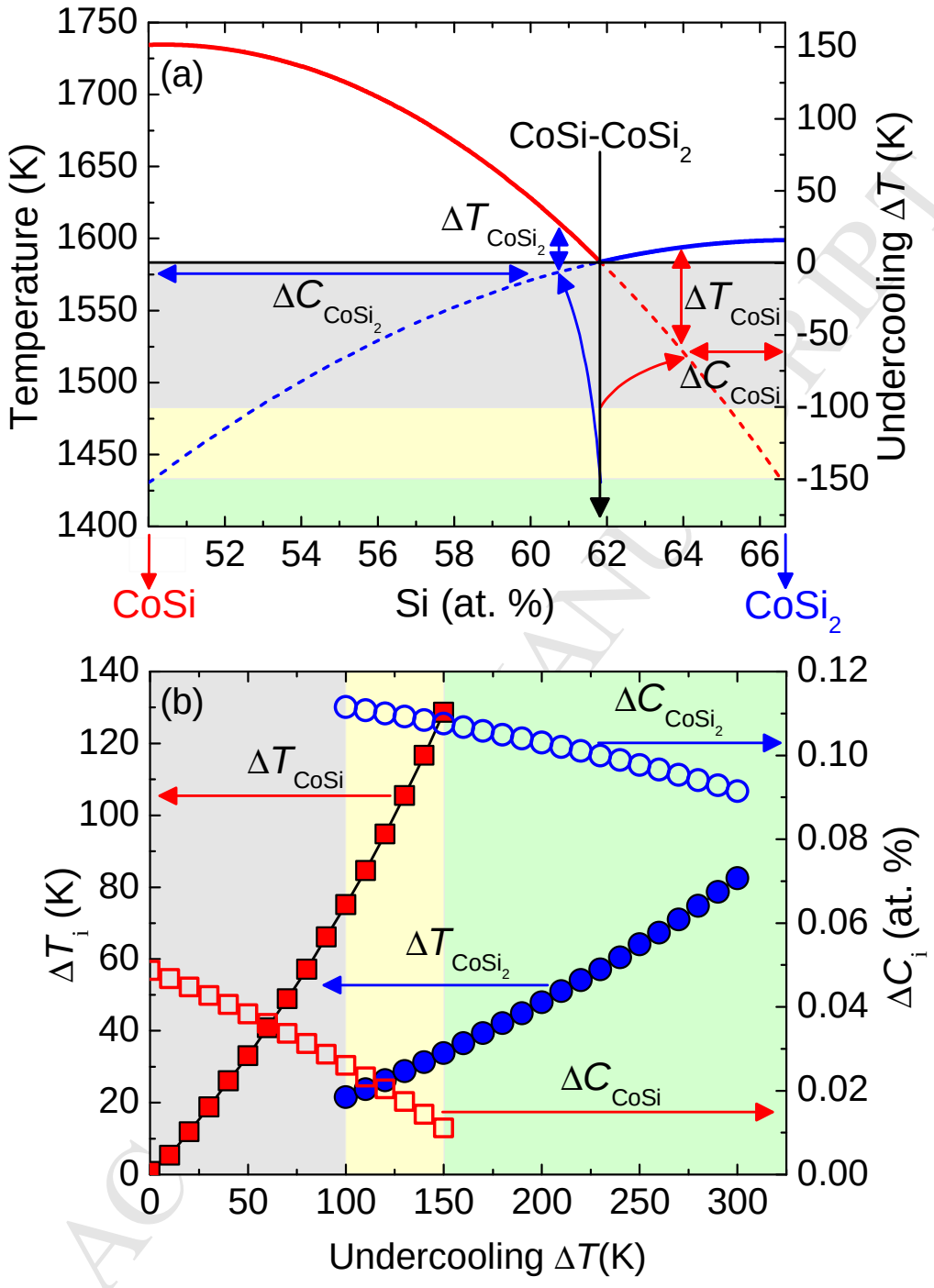

596

597 Fig. 4 (a) A partial Co–Si phase diagram [16]. Red and blue dashed lines indicate the
598 projected extension of the liquidus for CoSi and $CoSi_2$ in the undercooled region, respectively.
599 (b) Changes in the thermal driving force (ΔT_i) and solute concentration difference (ΔC_i) as a
600 function of undercooling for primary nucleation of CoSi and $CoSi_2$.

601 **Figure 5**

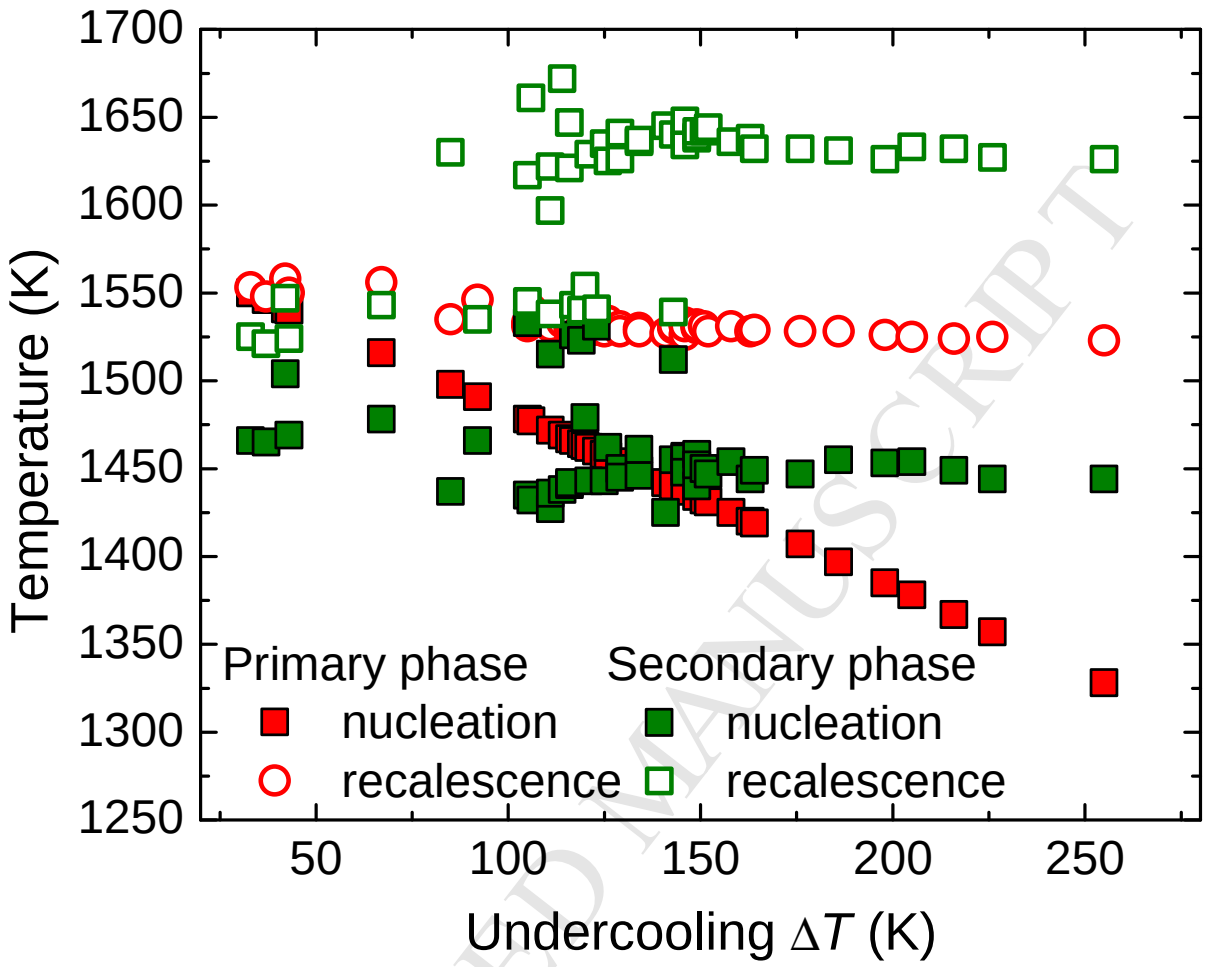

602

603 Fig. 5. Characteristic nucleation and recalescence temperatures of Co–61.8 at. % Si alloys
604 processed in ESL.

605

606 **Figure 6**

607 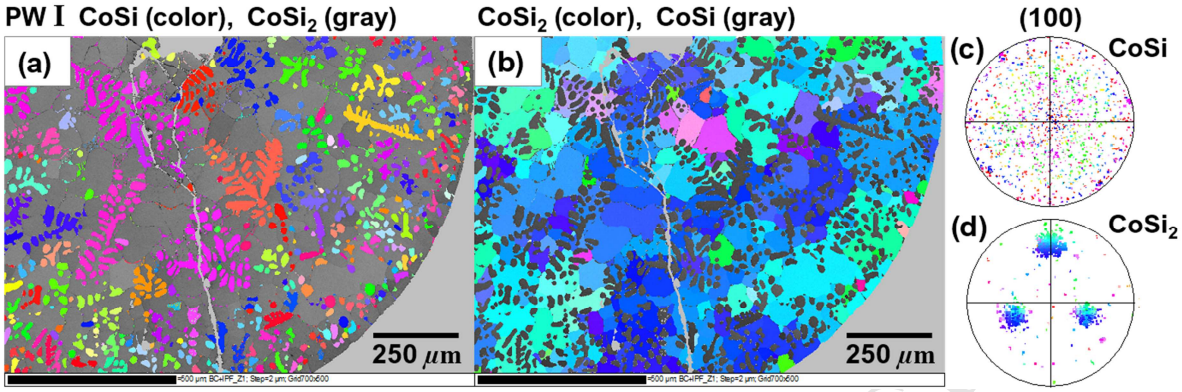

608 Fig. 6. Pathway (PW) I EBSD orientation maps colored for (a) CoSi and (b) $CoSi_2$ phases and

609 (100) pole figures for (c) the CoSi and (b) $CoSi_2$ phases, respectively.

610

611 **Figure 7**

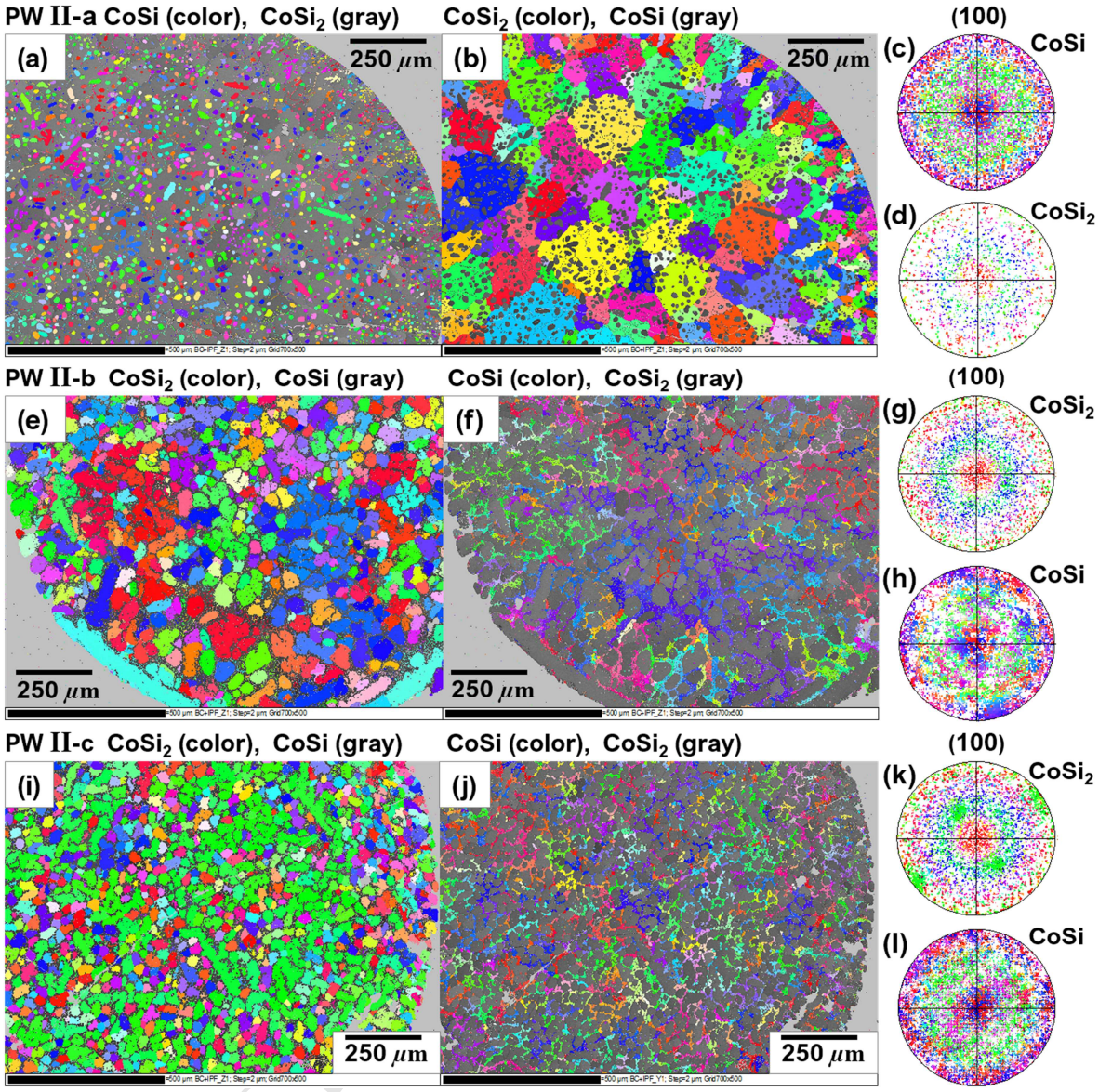

612

613 Fig. 7. Pathway (PW) II EBSD orientation maps for (a, f, j) CoSi and (b, e, i) $CoSi_2$ phases

614 and (100) pole figures of (c, h, l) the CoSi and (d, g, k) $CoSi_2$ phases, respectively.

615

616 **Figure 8**

617 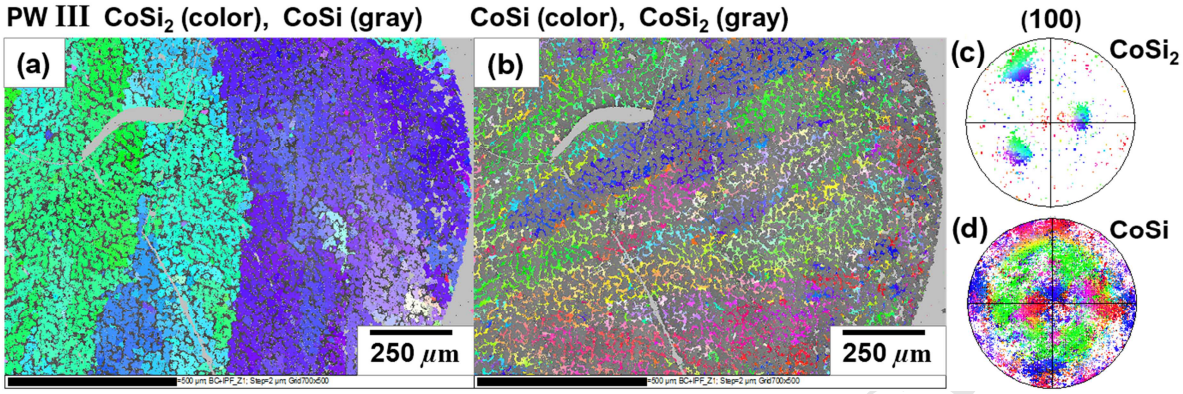

618 Fig. 8. Pathway (PW) III EBSD orientation maps for (a) $CoSi_2$ and (b) CoSi phases and (100)

619 pole figures for (c) the $CoSi_2$ and (b) CoSi phases, respectively.

620

621 **Figure 9**

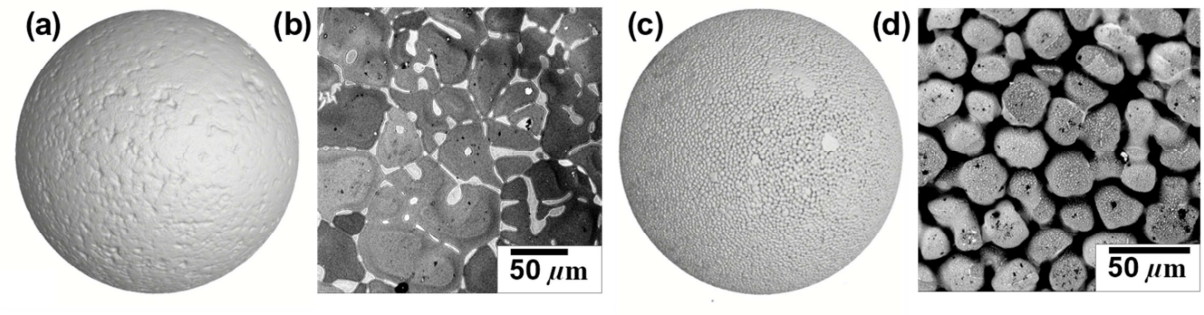

622

623 Fig. 9. (a and c) Images captured from tomography scans of the samples of pathways I and II-
624 c, respectively. (b and d) Back-scattered SEM images on the sample surfaces for pathways I
625 and II-c, respectively.

626

627 **Figure 10**

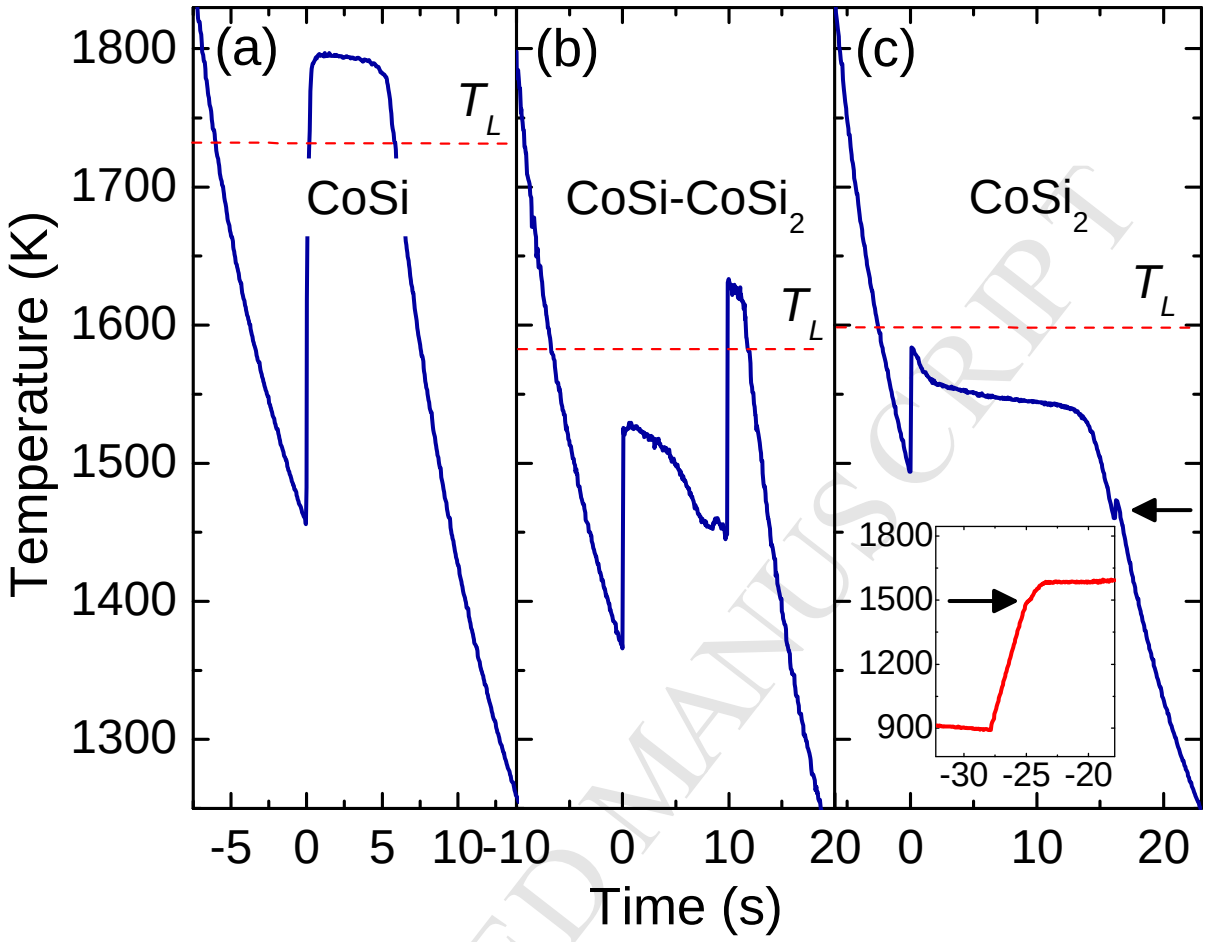

628

629 Fig. 10. Temperature-time profiles of three compositions in the ESL. (a) pure CoSi, (b)
630 eutectic CoSi–$CoSi_2$ mixture, and (c) pure $CoSi_2$; red dotted lines indicate the liquidus (T_L) of
631 each composition. Inset in (c) shows a heating curve for $CoSi_2$.

632

633 **Figure 11**

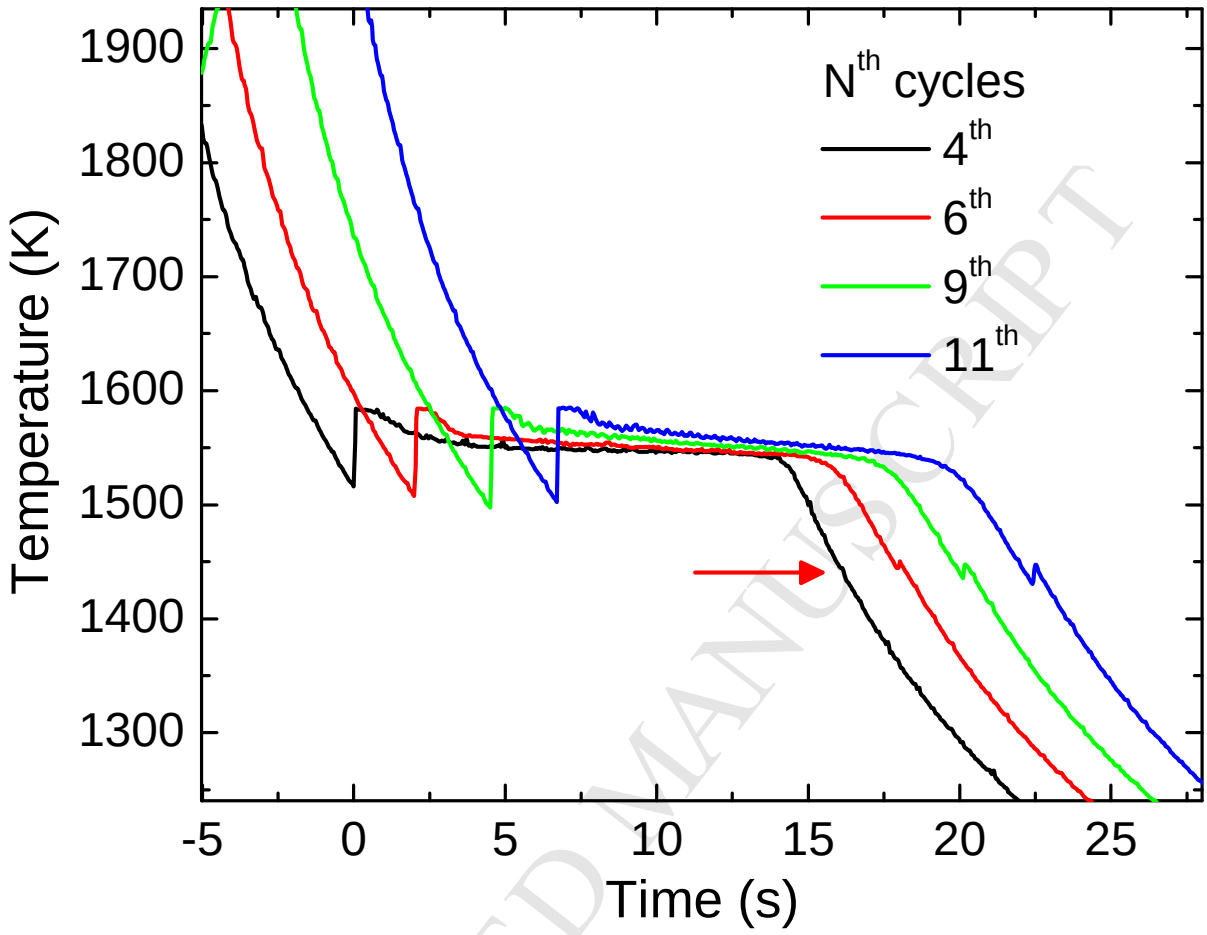

634

635 Fig. 11. Continuous thermal cycles of a single sample of $CoSi_2$ in the ESL. As the cycles are

636 repeated, a small peak (arrow) begins to gradually appear.

637